Supplementary information

for

Dyadic promotion of photocatalytic aerobic oxidation *via* the Mott-Schottky effect enabled by nitrogen-doped carbon from imidazolium-based ionic polymer

Hong Zhong,[a] Can Yang,[b] Lizhou Fan,[a] Zhihua Fu,[a] Xue Yang,[a] Xinchen Wang[b] and Ruihu Wang*[a]

[a] State Key Laboratory of Structural Chemistry, Fujian Institute of Research on the Structure of Matter, Chinese Academy of Sciences, Fuzhou, Fujian, 350002, China

[b] State Key Laboratory of Photocatalysis on Energy and Environment, College of Chemistry, Fuzhou University, Fuzhou, 350002, China.

Characterization Instrumentation: Fourier-transform infrared spectroscopy (FTIR) spectra were recorded with KBr pellets using Perkin-Elmer Instrument. Solid-state ^{13}C CP/MAS NMR was performed on a Bruker SB Avance III 500 MHz spectrometer with a 4-mm double-resonance MAS probe, a sample spinning rate of 7.0 kHz, a contact time of 2 ms and pulse delay of 5 s. Solid-state UV-vis spectroscopic analyses were performed on a Lambda 35 UV-vis spectrophotometer. Raman spectra were obtained using a Renishaw UV-1000 Photon Design spectrometer at 532 nm excitation focused through a 100 × microscope objective for a total interrogation spot size of ~1 μm. Powered X-ray diffraction (XRD) patterns were recorded in the range of $2\theta = 10\text{-}85^{o}$ on a desktop X-ray diffractometer (RIGAKU-Miniflex II) with Cu K_{α} radiation (λ = 1.5406 Å). Adsorption and desorption isotherms of nitrogen and hydrogen were measured at 77 K using a Micromeritics ASAP 2020 system. The samples were degassed at 120 ^{o}C for 10 h before the measurements. Surface areas were calculated from the adsorption data using Brunauer-Emmett-Teller (BET) and Langmuir methods. The pore size distribution curves were obtained from the adsorption branches using non-local density functional theory (NLDFT) method. Field-emission scanning electron microscopy (SEM) was performed on a JEOL JSM-7500F operated at an accelerating voltage of 3.0 kV. Transmission electron microscope (TEM) images were obtained with a JEOL JEM-2010 instrument operated at 200 kV. The cyclic voltammetry (CV) and Motte-Schottky measurements were performed using BAS 100B instrument, platinized platinum (0.5 cm^2) as the counter electrode, Ag/AgCl electrode as the reference electrode. Hall effect measurements were performed using HP-5500C instrument with a magnetic field of 0.5 T. X-ray photoelectron spectroscopy (XPS) measurements were performed on a Thermo ESCALAB 250 spectrometer, using non-monochromatic Al K_{α} X-rays as the excitation source and choosing C 1s (284.6 eV) as the reference line. The *I-V* curves were obtained on a CH Instruments by varying the voltage between ±2 V. Gas chromatography (GC) was performed on a Shimadzu GC-2014 equipped with a capillary column (RTX-5, 30 m × 0.25 μm) using a flame ionization detector. Inductively coupled plasma (ICP) measurement was performed on Jobin Yvon Ultima 2. The apparent quantum efficiency was measured under the normal reaction conditions, except the monochromatic LED lamps with different wavelength cutoff filter. The ILT 950 spectroradiometer was used to measure the intensity of incident

monochromatic illumination. Elemental analyses were performed on an Elementar Vario MICRO Elemental analyzer.

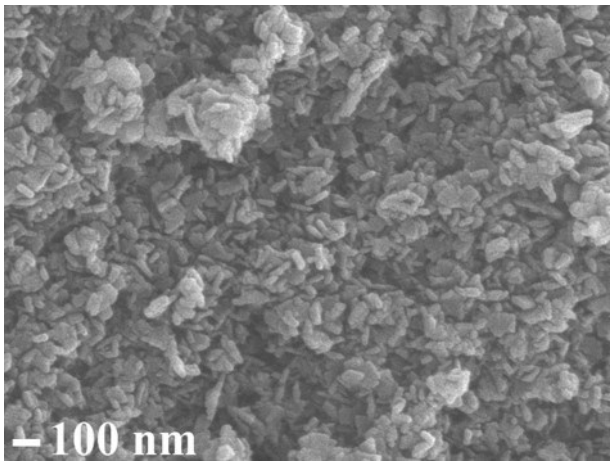

Fig.S1 SEM image of TiO_2.

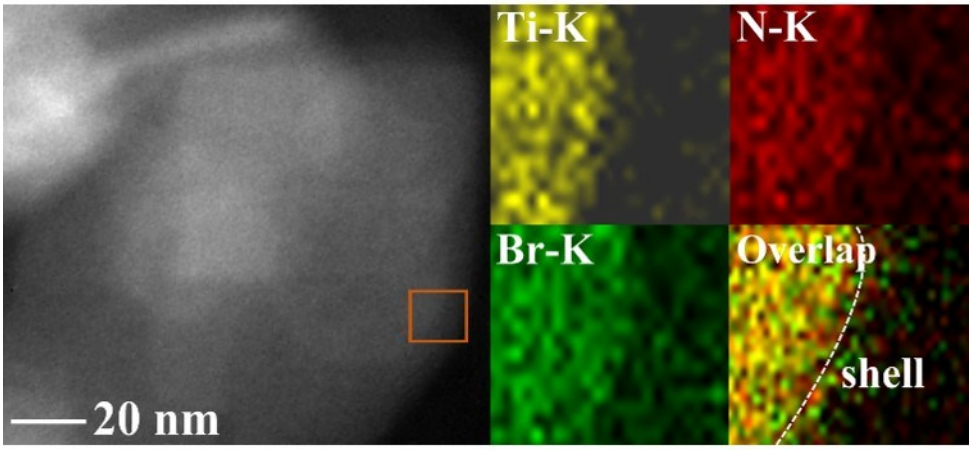

Fig. S2 HAADF-STEM and EDS elementary mapping images in the marked region for TiO_2@ImIP.

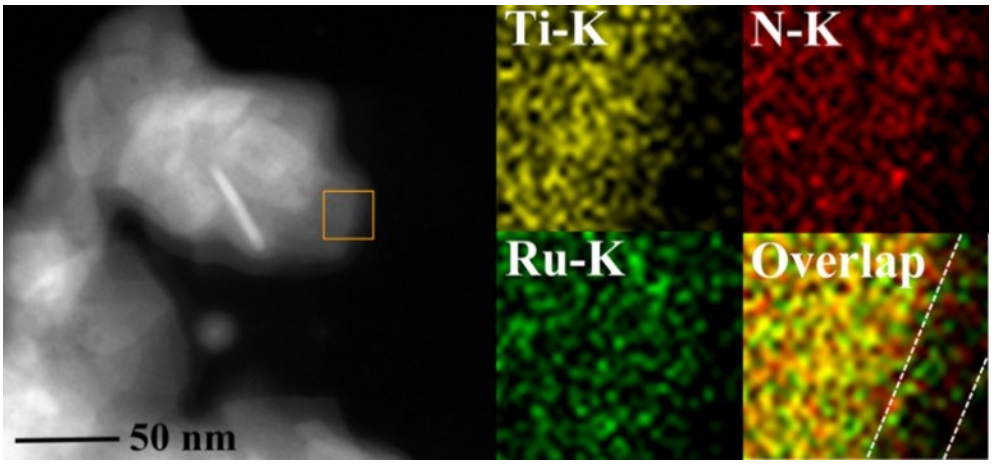

Fig. S3 HAADF-STEM and EDS elementary mapping images for TiO_2@ImIP-Ru.

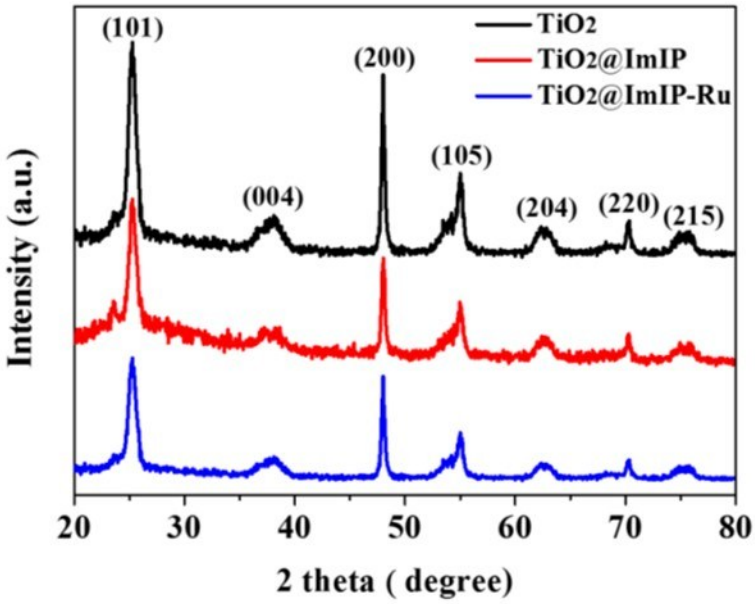

Fig. S4 XRD patterns of TiO_2, TiO_2@ImIP and TiO_2@ImIP-Ru.

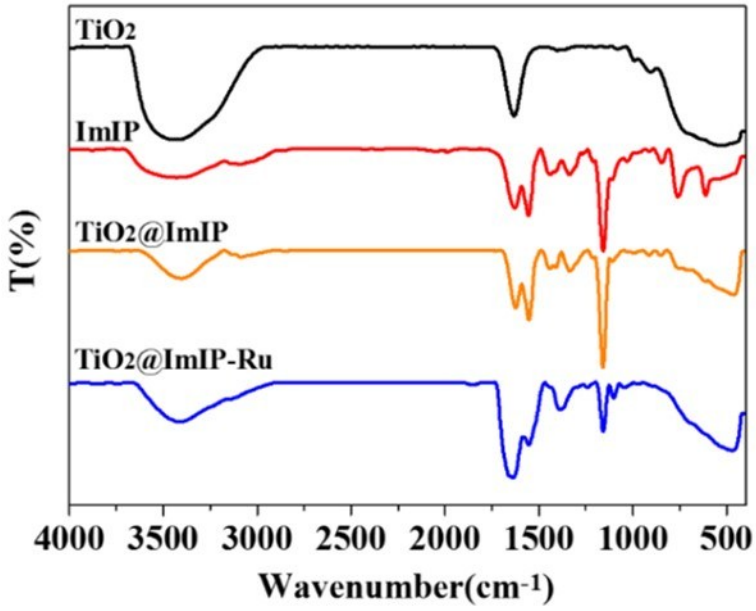

Fig. S5 FTIR spectra of TiO_2, ImIP, TiO_2@ImIP, TiO_2@ImIP-Ru.

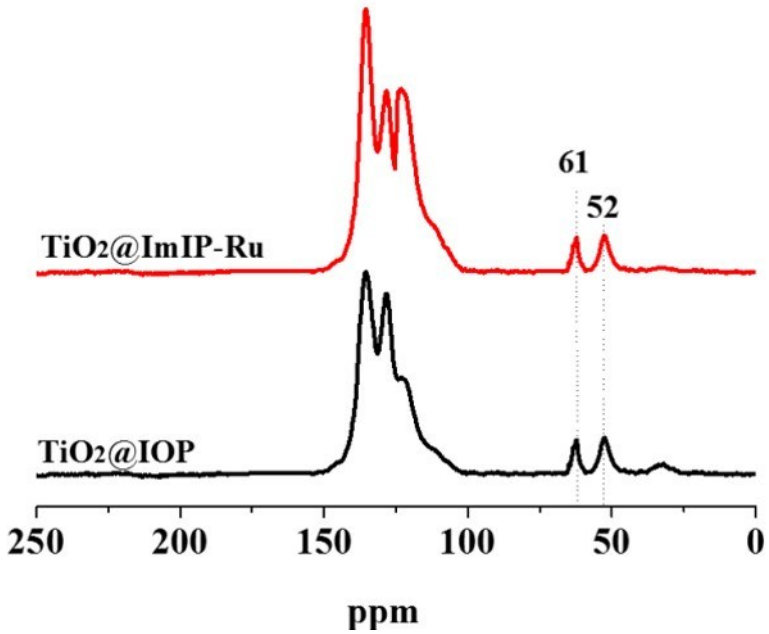

Fig. S6 The solid-state ^{13}C NMR spectra of TiO_2@ImIP and TiO_2@ImIP-Ru.

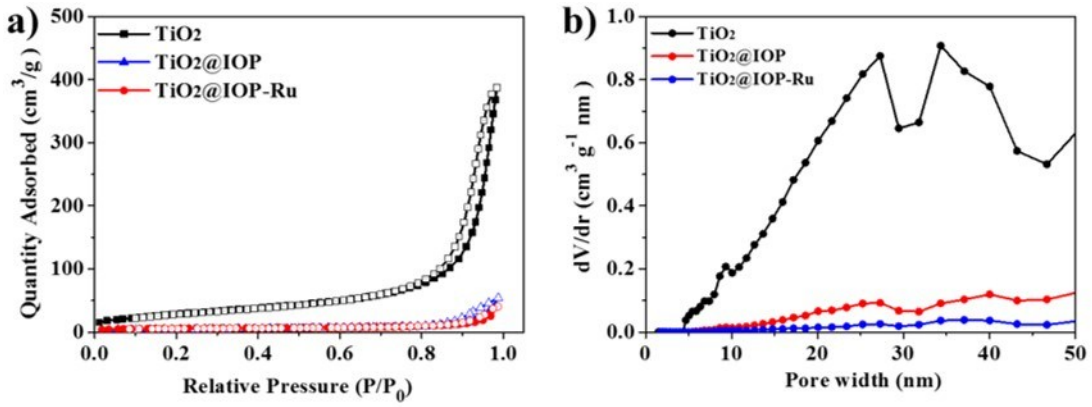

Fig. S7 (a) N_2 adsorption/desorption isotherms and (b) pore size distribution for TiO_2, TiO_2@ImIP and TiO_2@ImIP-Ru.

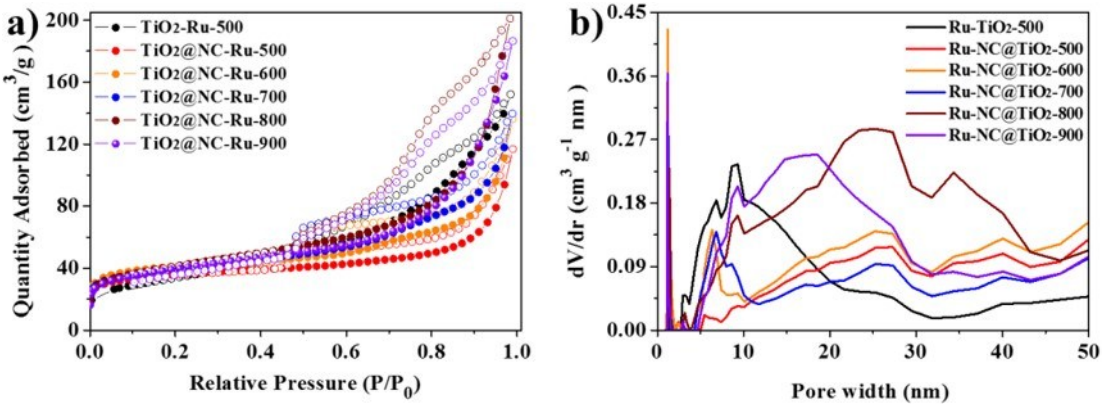

Fig. S8 (a) N_2 adsorption/desorption isotherms and (b) pore size distribution for TiO_2-Ru-500 and TiO_2@NC-Ru-T.

The porous properties of TiO_2, TiO_2@ImIP and TiO_2@ImIP-Ru were investigated by nitrogen physisorption at 77 K. As shown in Supplementary Fig. S7a, their nitrogen adsorption/desorption isotherms exhibit a type IV pattern according to the IUPAC classification[S1]. The apparent hysteresis at high relative pressure in TiO_2 indicates the presence of extensive mesopores, which probably originates from irregular stacking of TiO_2 nanosheets. Brunauer-Emmett-Teller (BET) surface area and total pore volume of TiO_2 are 108 m^2 g^{-1} and 0.60 m^3 g^{-1}, respectively. The pore size distribution further reveals that TiO_2 possesses predominantly mesopore (Supplementary Fig. S7b), which is in accordance with the result of nitrogen adsorption/desorption isotherm. The hysteresis in the sorption isotherms of TiO_2@ImIP and TiO_2@ImIP-Ru is remarkably shrunk in comparison with that of TiO_2. The nitrogen uptake amounts are decreased sharply from 388 cm^3 g^{-1} in TiO_2 to

54 cm^3 g^{-1} in TiO_2@ImIP and 41 cm^3 g^{-1} in TiO_2@ImIP-Ru. The BET surface areas of TiO_2@ImIP and TiO_2@ImIP-Ru are reduced to 36 and 23 m^2 g^{-1}, respectively, and their total pore volume are significantly decreased to 0.084 and 0.076 m^3 g^{-1}, respectively, which are attributed to both partial pore filling and mass increment after ImIP encapsulation and subsequent anion exchange. It should be mentioned that the contribution of microporosity to total pore volume is negligible in TiO_2, TiO_2@ImIP and TiO_2@ImIP-Ru.

The porous properties of TiO_2@NC-Ru-T were also investigated by nitrogen physisorption at 77 K (Supplementary Fig. S8a). The nitrogen adsorption-desorption isotherms of TiO_2@NC-Ru-T exhibit a combination pattern of type I and IV [S1]. The rapid nitrogen uptake at very low relative pressure ($P/P_0 < 0.01$) suggests the presence of micropore, which is attributed to the intrinsic micropore of nitrogen-doped carbon. The obvious hysteresis at high relative pressure indicates the presence of extensive mesopore, which originates from both partial stacking of nanosheets and intrinsic mesopore of nitrogen-doped carbon. BET surface area and total pore volume in TiO_2@NC-Ru-T are in the range from 131 to 148 m^2 g^{-1} and from 0.18 to 0.39 cm^3 g^{-1}, respectively (Table S1), which are much higher than corresponding those in TiO_2, TiO_2@ImIP and TiO_2@ImIP-Ru. The pore size distribution further reveals the presence of micropore and mesopore in TiO_2@NC-Ru-T, which is consistent with the N_2 isotherm results (Supplementary Fig. S8b). In sharp contrast, the nitrogen adsorption-desorption isotherm of TiO_2-Ru-500 exhibits a type IV pattern, which is similar to that of TiO_2 except with lower nitrogen uptake amount, indicating the retention of the mesopore structure after the loading of Ru NPs. BET surface area and total pore volume in TiO_2-Ru-500 are 87 m^2 g^{-1} and 0.24 cm^3 g^{-1}, respectively, which are lower than that of TiO_2 due to both partial pore filling and mass increment after Ru loading. These results reveal that the introduction of nitrogen-doped carbon materials is favorable for porous properties of photocatalysts.

Table S1. The texture properties and the compositions for TiO_2@NC-Ru-T.

Samples	S_{BET} (m^2 g^{-1})[a]	V_{Total} (cm^3 g^{-1})[a]	Ru NPs size (nm)[b]	Ru loading (mmol g^{-1})[c]	C content[d]	N content[d]	I_D/I_G[e]
TiO_2@NC-Ru-500	131	0.18	1.90±0.20	0.293	15.13	1.75	1.16
TiO_2@NC-Ru-600	136	0.21	2.35±0.20	0.312	12.51	1.22	1.05
TiO_2@NC-Ru-700	142	0.27	2.85±0.40	0.326	12.19	1.01	0.96
TiO_2@NC-Ru-800	146	0.31	3.20±0.50	0.346	11.57	0.79	0.91
TiO_2@NC-Ru-900	148	0.39	3.90±0.50	0.363	11.15	0.39	0.87
TiO_2-Ru-500	87	0.24	-	0.280	-	-	

[a]Calculated from nitrogen adsorption/desorption isotherms; [b]Determined by TEM analyses; [c]Determined by ICP analyses; [d]Determined by elementary analyses; [e]Calculated from the Raman spectra.

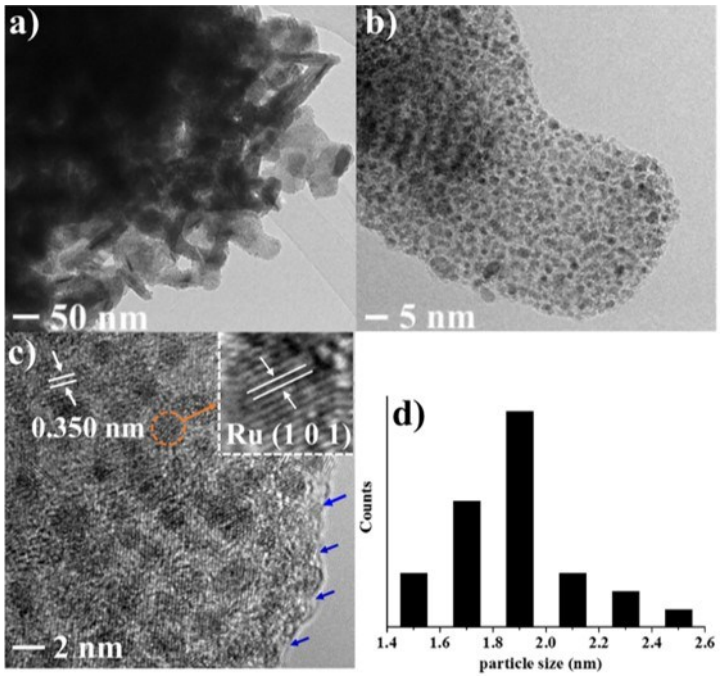

Fig. S9 (a, b) TEM images, (c) HRTEM image and (d) the size distribution of Ru NPs for TiO_2@NC-Ru-500. Blue arrows in c are indicative of NC.

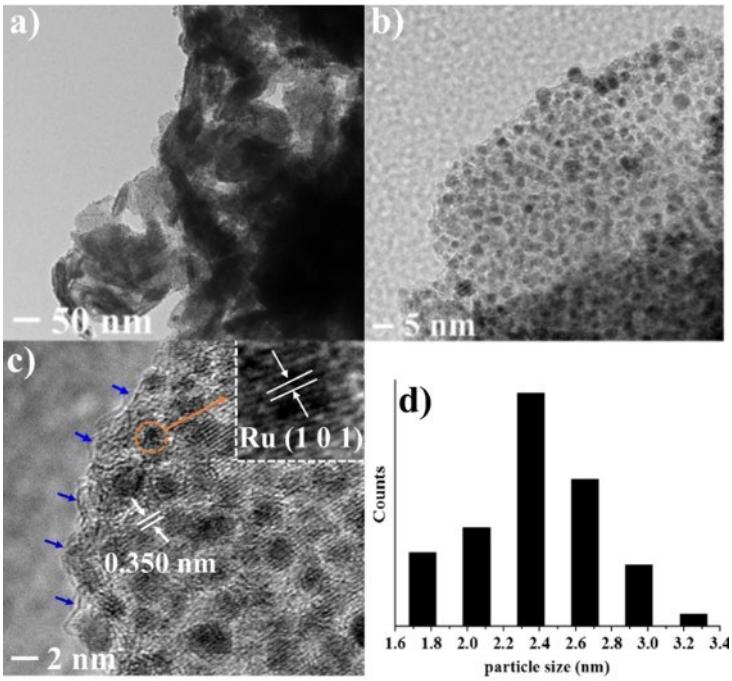

Fig. S10 (a, b) TEM images, (c) HRTEM image and (d) the size distribution of Ru NPs for TiO_2@NC-Ru-600. Blue arrows in c are indicative of NC.

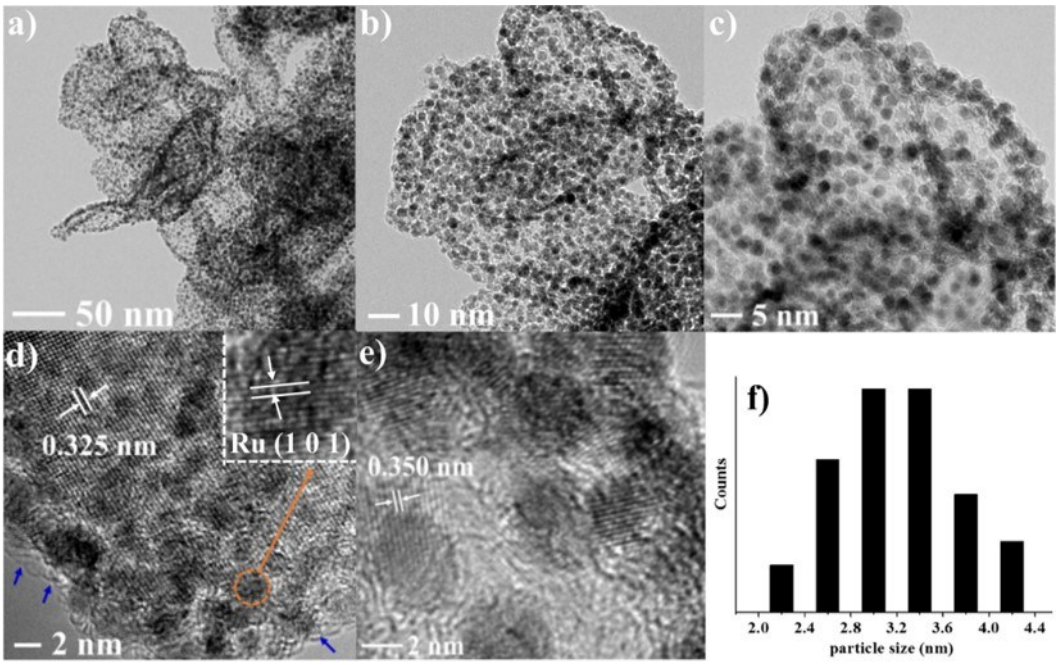

Fig. S11 (a, b, c) TEM images, (d, e) HRTEM images and (f) the size distribution of Ru NPs for TiO_2@NC-Ru-800. Blue arrows in d are indicative of NC.

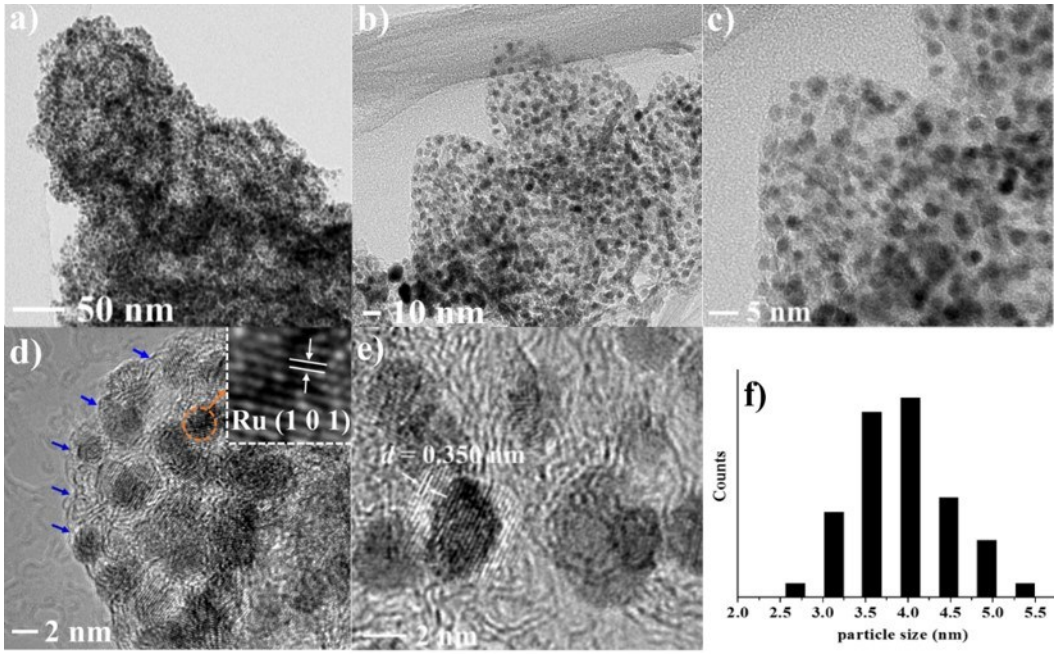

Fig. S12 (a, b, c) TEM images, (d, e) HRTEM images and (f) the size distribution of Ru NPs for TiO_2@NC-Ru-900. Blue arrows in d are indicative of NC.

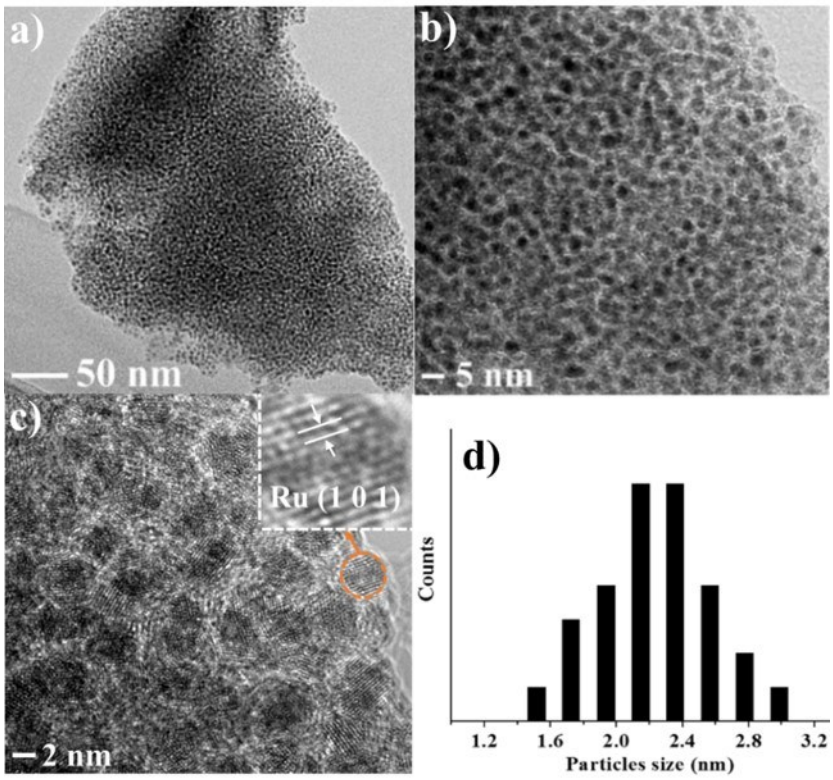

Fig. S13 (a, b) TEM images, (c) HRTEM image and (d) the size distribution of Ru NPs for NC-Ru-700.

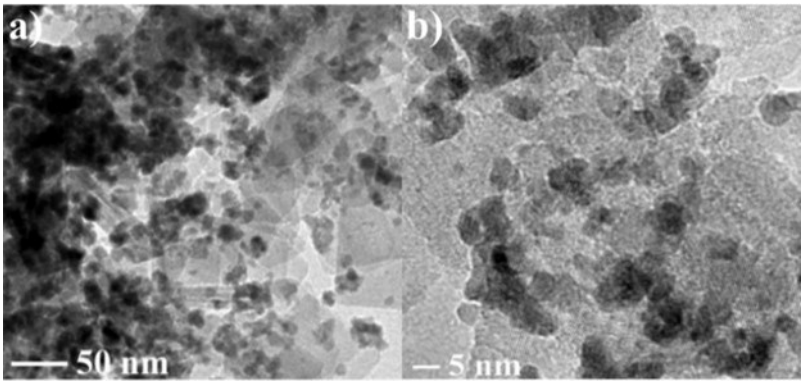

Figure S14. TEM images for TiO_2-Ru-500.

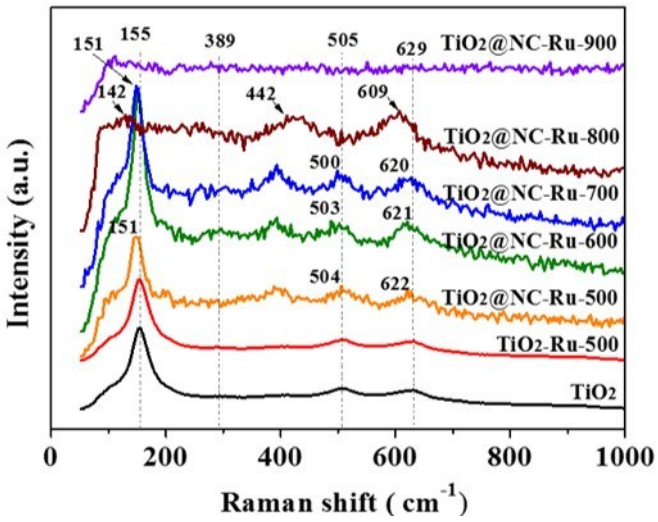

Fig. S15 Raman spectra for TiO_2, TiO_2-Ru-500 and TiO_2@NC-Ru-T in the range of 50-1000 cm^{-1}.

The Raman spectra of the TiO_2 nanosheets, TiO_2-Ru-500 and TiO_2@NC-Ru-T are shown in Fig. 4b. TiO_2-Ru-500 shows the characteristic peaks of anatase at 155, 389, 505 and 630 cm^{-1}, which are almost identical with that of the TiO_2 nanosheets [S2-S4], indicating the loading of Ru NPs has negligible effect on the TiO_2 nanosheets. The peaks in the Raman spectra of TiO_2@NC-Ru-500, TiO_2@NC-Ru-600 and TiO_2@NC-Ru-700 are similar to those of TiO_2 and Ru@TiO_2 in the range of 50-1000 cm^{-1} except with a slight red shift, further indicating the anatase phase of TiO_2 are intact after pyrolysis at 700 ^oC (Supplementary Fig. S15). The red shift of the Raman peaks indicates that a more strong interaction between nitrogen-doped carbon and TiO_2[S2]. It should be mentioned that the TiO_2@NC-Ru-800 shows distinctly different peaks at 142, 442 and 609 cm^{-1}, which suggests that the phase transformation of the TiO_2 nanosheeets from anatase to rutile during pyrolysis at 800 ^oC[S2]. The total disappearance of characteristic peaks in the range of 50-1000 cm^{-1} indicates that TiO_2@NC-Ru-900 is mainly composed of amorphous TiO_2. These Raman spectra analyses are entirely consistent with their XRD results and TEM observations.

The roles of the carbon materials in TiO_2@NC-Ru-T were also disclosed by Raman spectroscopy. All samples show the characteristic D-band and G-band of the carbon species at 1346 and 1588 cm^{-1}, respectively. The intensity ratio of D-band/G-band is indicative of the degree of graphitization. As shown in Table S1, the ratios gradually decrease from 1.16 in TiO_2@NC-Ru-500 to 0.87 in TiO_2@NC-Ru-900 with

increasing pyrolysis temperature of TiO_2@ImIP-Ru. This result is in good agreement with the observation of TEM images.

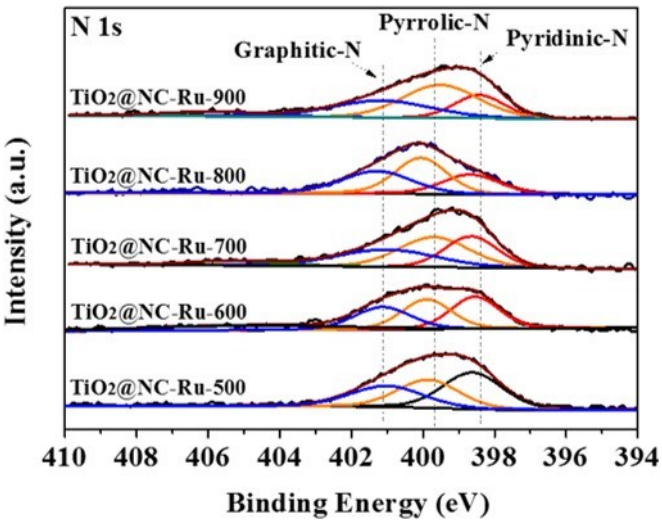

Fig. S16 N 1s XPS spectra of TiO_2@NC-Ru-T.

The surface compositions in TiO_2@NC-Ru-T were investigated by X-ray photoelectron spectroscopy (XPS). As shown in Fig. 4c, the overlapping of C ls emission and the Ru $3d_{3/2}$ component at 284.8 eV makes unequivocal determination difficult, but the deconvolution of Ru 3d XPS spectra provides two sets of double peaks corresponding to Ru $3d_{5/2}$ and Ru $3d_{3/2}$. The binding energy peaks of Ru $3d_{5/2}$ at 280.28 and 281.39 eV in TiO_2@NC-Ru-T are assigned to Ru(0) and Ru (δ^+) species[S5], respectively. The pyrolysis temperatures have no apparent effect on the Ru 3d binding energy peaks. However, the binding energy peak of Ru(0) $3d_{5/2}$ in TiO_2-Ru-500 occurs at 280.70 eV, the negative shift by 0.42 eV in TiO_2@NC-Ru-T suggests the strong interaction between Ru NPs and nitrogen-doped carbon, in which the electron donation from N-doped carbon to Ru NPs makes Ru species more electron-rich. In the high-resolution N 1s XPS spectra of TiO_2@NC-Ru-T, the presence of pyridinic N (398.5 eV), pyrrolic N (399.7 eV) and graphitic N (401.1 eV) could be clearly identified (Supplementary Fig. S16)[S6], which is consistent with HRTEM observations and Raman results.

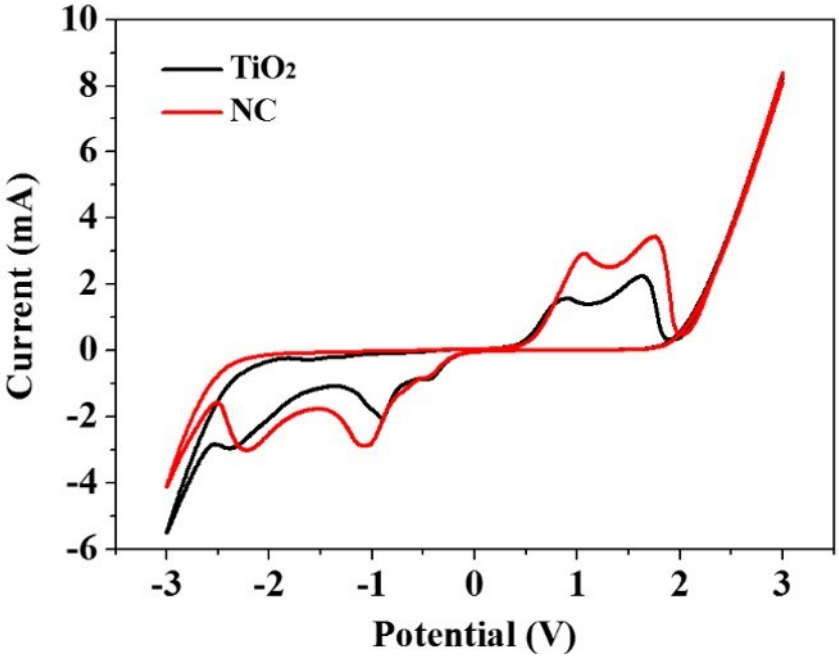

Fig. S17 Cyclic voltammetry curves for TiO_2 and NC.

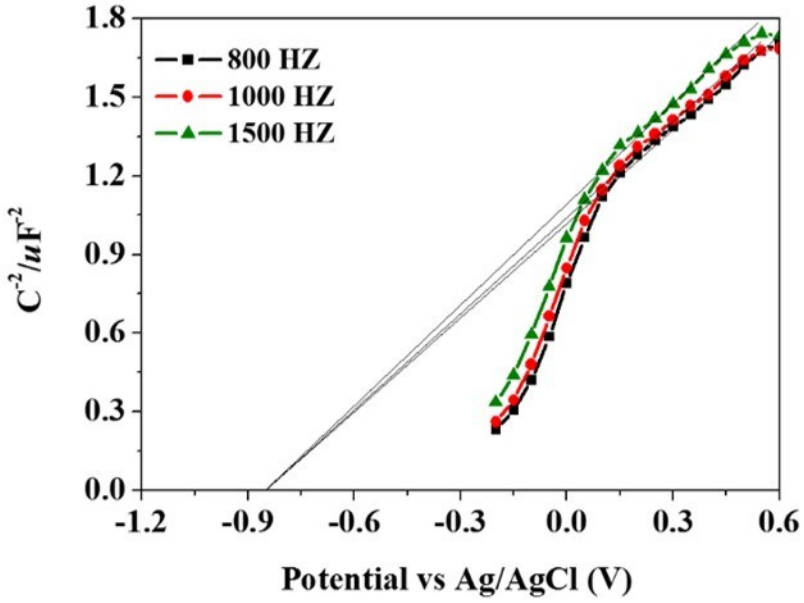

Fig. S18 Mott-Schottky plots of TiO_2 nanosheet.

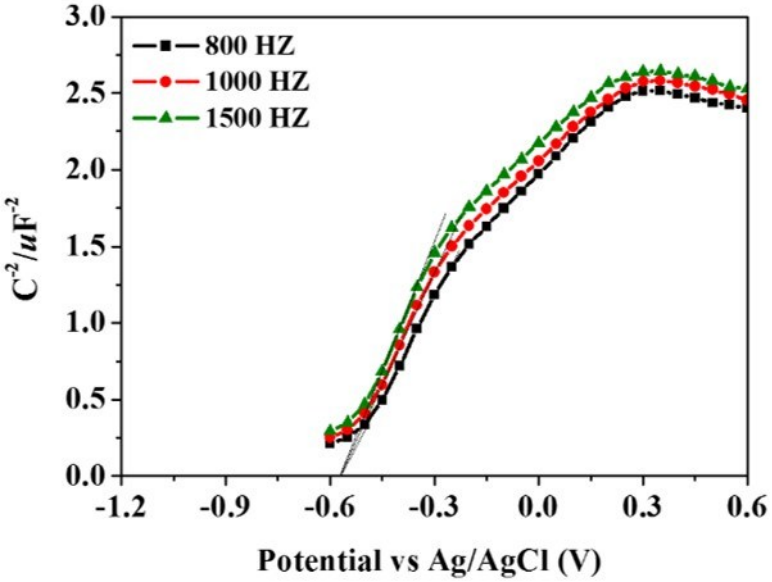

Fig. S19 Mott-Schottky plots of NC.

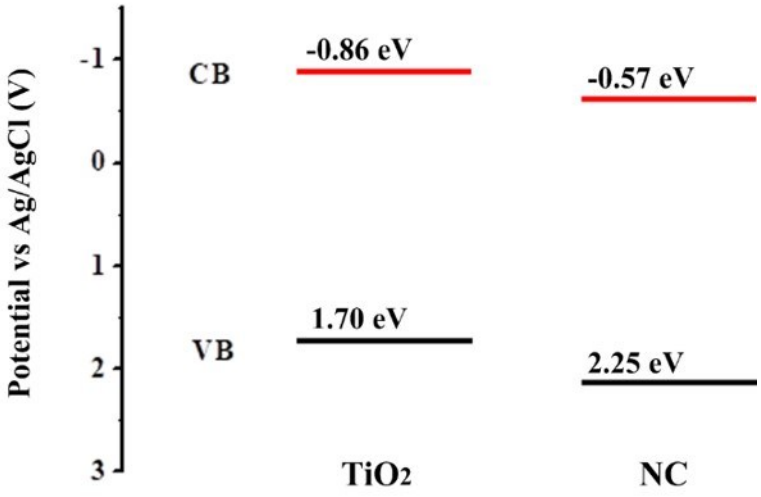

Fig. S20 The energy band structure of NC and TiO_2.

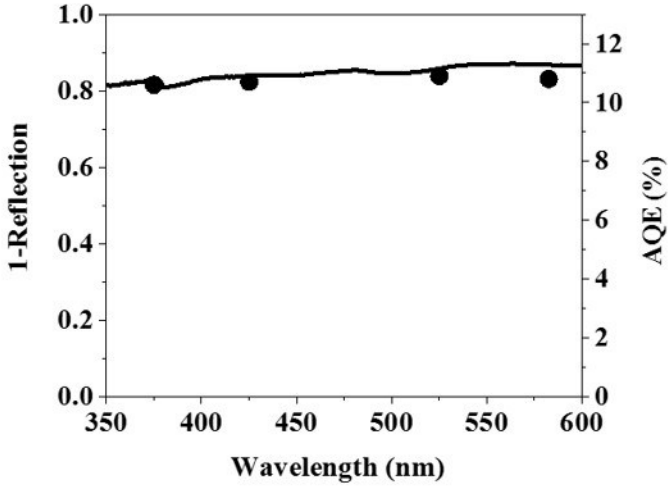

Fig. S21 Action spectrum for the photocatalytic oxidation of benzyl alcohol in TiO_2@NC-Ru-700.

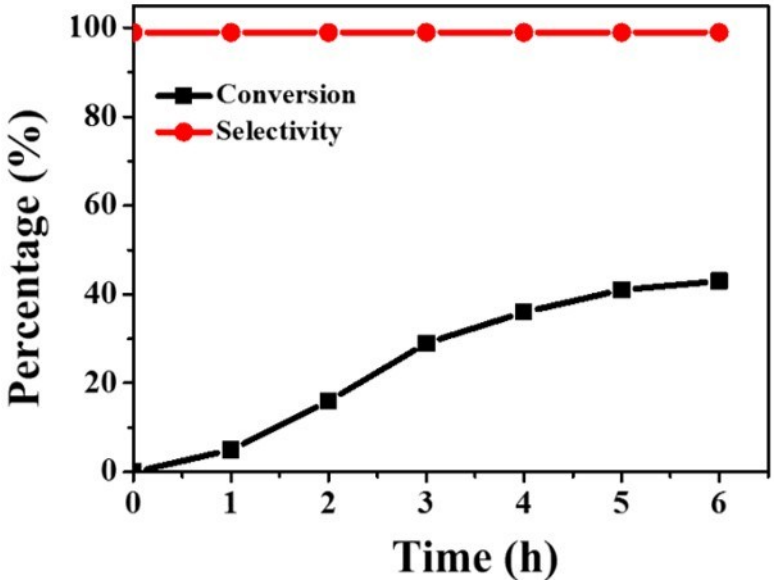

Fig. S22 The kinetic curve for TiO_2@NC-Ru-700 in the photocatalytic oxidation of benzyl alcohol under visible light irradiation. Reaction conditions: benzyl alcohol (0.5 mmol), Ru (1.0 mol%), H_2O (1 mL), air (1 atm) and 25 ^oC.

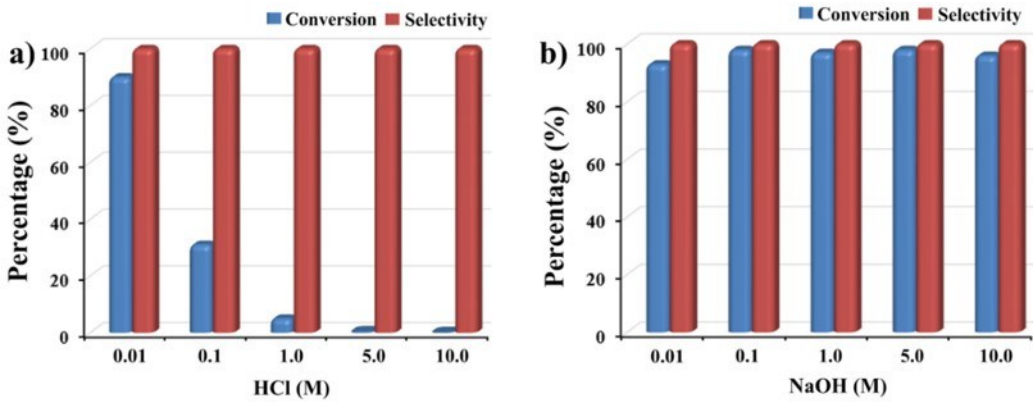

Fig. S23 The catalytic activity and selectivity of TiO_2@NC-Ru-700 in the aerobic oxidation of benzyl alcohol under acid and alkaline environment. Reaction conditions: benzyl alcohol (0.5 mmol), Ru (1.0 mol%), aqueous solution (1 mL), air (1 atm) and direct visible light exposure (56 ^oC).

The photocatalytic activities of TiO_2@NC-Ru-700 in the aerobic oxidation of benzyl alcohol were investigated under acid and alkaline conditions. The conversions of benzyl alcohol has no appreciable change in 0.01 M of aqueous HCl solution, while the use of 0.1 M and 1.0 M of aqueous HCl solution result in rapid decrement of the catalytic activity to 33% and 5%, respectively. The negligible conversion is detected in 5.0 M and 10.0 M of HCl aqueous solution (Fig. S22a, ESI†). However, the alkaline environment is beneficial for the catalytic reaction, and the conversions of benzyl alcohol in 0.01 and 0.1 M of aqueous NaOH solution increase to 94% and 99%, respectively, further increment of basicity has no obvious effect on the reaction (Fig. S22b, ESI†). It should mentioned that the selectivity remains above 99% both in acid and alkaline environment.

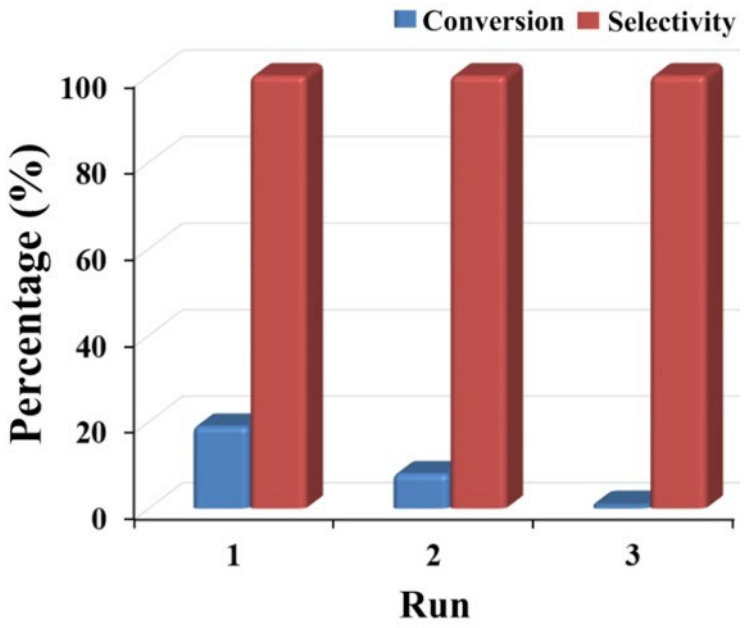

Fig. S24 Recyclability of TiO_2-Ru-500 in the aerobic oxidation of benzyl alcohol upon direct visible light exposure; Reaction conditions: benzyl alcohol (0.5 mmol), Ru (1.0 mol%), H_2O (1 mL), air (1 atm), upon direct visible light exposure, 6 h.

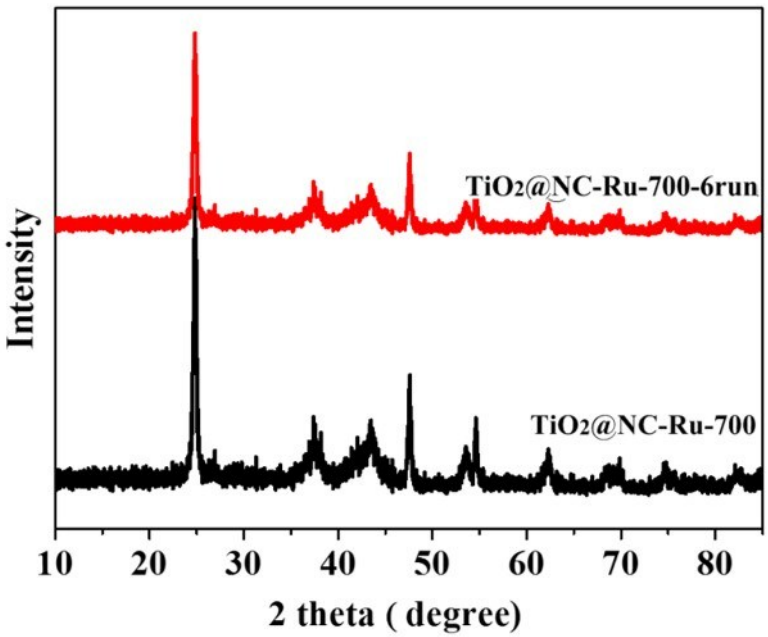

Fig. S25 XRD patterns of TiO_2@NC-Ru-700 and TiO_2@NC-Ru-700-6run.

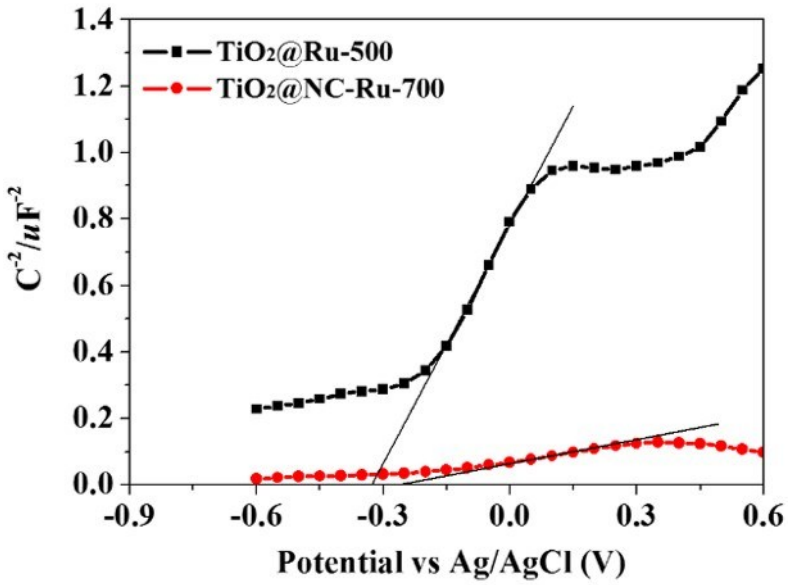

Fig. S26 Mott-Schottky plots of TiO_2@-Ru-500 and TiO_2@NC-Ru-700 at the frequency of 1 kHz

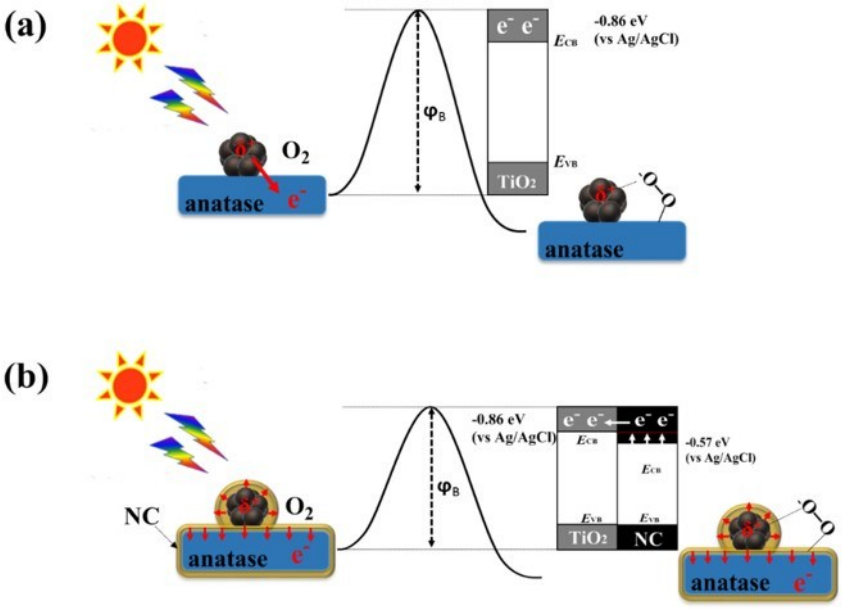

Fig. 27 The photoelectron transfer mechanism in (a) TiO_2@-Ru-500 and (b) TiO_2@NC-Ru-700.

References

S1 G. L. Aranovich and M. D.Donohue, *Adv. Colloid Interface,* 1998, **77**, 137-152.

S2 L. W. Zhang, H. B. Fu and Y. F. Zhu, *Adv. Funct. Mater.,* 2008, **18**, 2180-2189.

S3 L. Wu, D. Bresser, D. Buchholz, G. A. Giffin, C. R. Castro, A. Ochel and S. Passerini, *Adv. Energy Mater.,* 2015, **5**, 1401142.

S4 J. Wang, H. Wu, D. Gao, S. Miao, G. Wang and X. Bao, *Nano Energy,* 2015, **13**, 387-396

S5 V. V. Costa, M. J. Jacinto, L. M. Rossi, R. Landers and E. V.Gusevskaya, *J. Catal.* 2011, **282**, 209-214.

S6 L. Li, C. Cui, H. Fan and R. Wang, *ChemSusChem,* 2017, **10**, 4921-4926.